JGR Space Physics

RESEARCH ARTICLE
10.1029/2024JA033051

Nightside Electron Precipitation Patterns as Observed by ELFIN and CIRBE CubeSats

Kun Zhang[1], **Anton V. Artemyev**[1], **Xinlin Li**[2,3], **Xiao-Jia Zhang**[1,4], **Vassilis Angelopoulos**[1], **Yang Mei**[2,3], **Zheng Xiang**[2], and **Niklas Grimmich**[5]

[1]Department of Earth, Planetary, and Space Sciences, University of California, Los Angeles, Los Angeles, CA, USA, [2]Laboratory for Atmospheric and Space Physics, University of Colorado Boulder, Boulder, CO, USA, [3]Department of Aerospace Engineering Sciences, University of Colorado Boulder, Boulder, CO, USA, [4]Department of Physics, University of Texas at Dallas, Richardson, TX, USA, [5]Institut für Geophysik und Extraterrestrische Physik, Technische Universität Braunschweig, Braunschweig, Germany

Key Points:

- ELFIN observations reveal features of isotropy boundary and EMIC-driven precipitation in locally-trapped electron measurements
- We develop a method for identifying isotropy boundary and EMIC-driven precipitation using locally-trapped flux by CIRBE
- We report a substorm event with electron precipitation by curvature scattering and EMIC wave scattering observed by CIRBE

Correspondence to:
K. Zhang,
kzhang@epss.ucla.edu

Citation:
Zhang, K., Artemyev, A. V., Li, X., Zhang, X.-J., Angelopoulos, V., Mei, Y., et al. (2024). Nightside electron precipitation patterns as observed by ELFIN and CIRBE CubeSats. *Journal of Geophysical Research: Space Physics*, *129*, e2024JA033051. https://doi.org/10.1029/2024JA033051

Received 10 JUL 2024
Accepted 24 OCT 2024

Abstract

The rapidly expanding fleet of low-altitude CubeSats equipped with energetic particle detectors brings new opportunities for monitoring the dynamics of the radiation belt and near-Earth plasma sheet. Despite their small sizes, CubeSats can carry state-of-the-art instruments that provide electron flux measurements with finer energy resolution and broader energy coverage, compared to conventional missions such as POES satellites. The recently launched CIRBE CubeSat measures 250–6,000 keV electrons with extremely high energy resolution, however, CIRBE typically only measures locally-trapped electrons and cannot directly measure the precipitating electrons. This work aims to develop a technique for identifying indications of nightside precipitation using the locally-trapped electron measurements by the CIRBE CubeSat. This study focuses on two main types of drivers for nightside precipitation: electron scattering by the curvature of magnetic field lines in the magnetotail current sheet and electron scattering by resonance with electromagnetic ion cyclotron (EMIC) waves. Using energy and pitch-angle resolved electron fluxes from the low-altitude ELFIN CubeSat, we reveal the features that distinguish between these two precipitation mechanisms based solely on locally-trapped flux measurements. Then we present measurements from four CIRBE orbits and demonstrate the applicability of the proposed technique to the investigation of nightside precipitation using CIRBE observations, enabling separation between precipitation induced by curvature scattering and EMIC waves in nearby regions. Our study underscores the feasibility of employing high-energy-resolution CIRBE measurements for detecting nightside precipitation of relativistic electrons. Additionally, we briefly discuss outstanding scientific questions about these precipitation patterns that could be addressed with CIRBE measurements.

1. Introduction

Precipitation into the Earth's ionosphere is an important loss mechanism of the magnetospheric electrons. There are two main mechanisms that can effectively scatter energetic electrons into the loss cone and cause enhanced precipitation: wave-particle resonant interactions (R. Millan & Thorne, 2007; Shprits et al., 2008) and electron scattering by magnetic field line curvature (Yahnin et al., 2016, 2017). Field line curvature scattering happens predominantly around midnight, where the highly curved magnetic field associated with the magnetotail current sheet can approach the geostationary orbit and induce long-term precipitation of energetic electrons within the transition region between the outer radiation belt and plasma sheet (Murase et al., 2022; Newell et al., 1998; Sergeev et al., 2012; Sivadas et al., 2019). As a result, the ratio of the precipitating electron fluxes to the trapped fluxes is often observed to be close to unity at low altitudes in this transition region, and the equatorward boundary of the precipitation region is known as the isotropy boundary (IB), the location of which is strongly dependent on energy (Imhof et al., 1977; Sergeev et al., 1983). The net electron loss associated with IB accounts for a significant fraction of the nightside (and total) electron loss of the outer radiation belt (Wilkins et al., 2023). Unlike wave-particle interactions that only take effect in a limited energy range, electron precipitation caused by curvature scattering at the IB can cover a wide energy range from ~100 keV to multi-MeV (Imhof et al., 1979). Consequently, curvature scattering or IB competes with electron scattering caused by electromagnetic whistler-mode waves at sub-relativistic energies (Artemyev, Neishtadt, & Angelopoulos, 2022; Gao et al., 2023; Tsai et al., 2022) and electromagnetic ion cyclotron (EMIC) waves at relativistic energies (Artemyev et al., 2023; Capannolo, Li, Millan, et al., 2022; H. Chen et al., 2023; Miyoshi et al., 2008; Nakamura et al., 2022; Shekhar et al., 2017; Yahnin et al., 2016) for the loss of magnetospheric electrons. Numerous efforts have been made to simulate wave-particle interactions and their contribution to the radiation belt dynamics (see reviews by Li & Hudson, 2019; Thorne et al., 2021, and references therein); however, there are still gaps in our understanding of the characterization and quantification of the electron precipitation loss associated with IB.

Establishing reliable methods for estimating the field line curvature from near-equatorial spacecraft measurements is the major challenge in the investigation of electron curvature scattering. The primary approaches here include estimating the magnetic field gradients using multi-spacecraft measurements (Artemyev et al., 2016; Sergeev et al., 2011; Tan et al., 2023; Vallat et al., 2005) and reconstructing the magnetic field configuration using event-oriented empirical models (Kubyshkina et al., 2009, 2011; Sergeev et al., 2023) or machine learning algorithms (Stephens et al., 2016, 2019). However, these two methods are not yet generalized for the statistical investigation of IB locations and the efficiency of curvature scattering in energetic electron precipitation. Currently, the most promising and widely used approach is through the detection of IB regions at low altitudes (Dubyagin et al., 2002; Sergeev et al., 1993, 2015). Measurements from the Polar Operational Environmental Satellites (POES) have been extensively studied for the determination of IBs (e.g., Capannolo, Li, Millan, et al., 2022; Yahnin et al., 2016, etc.), but their limited number of energy channels and energy coverage (Evans & Greer, 2004) make POES satellites nonideal for resolving the energy-dispersive IB characteristics in the radiation belt. This gap can be filled by recent low-altitude CubeSat missions such as the Electron Losses and Fields Investigation (ELFIN; see Angelopoulos et al., 2020), the Colorado Inner Radiation Belt Experiment (CIRBE; see Li et al., 2022, 2024), and the future Realistic Electron Atmospheric Loss (REAL; see R. Millan et al., 2021, 2022). These new CubeSats are equipped with new-generation energetic particle detectors and can provide electron measurements with fine energy resolution. Indeed, 3 years of ELFIN measurements have generated a comprehensive data set of electron IBs, revealing detailed characteristics such as the occurrence rate, spatial dependence and geomagnetic activity dependence (Wilkins et al., 2023). With the end of ELFIN era, CIRBE and REAL may continue to measure the nightside electron precipitation driven by curvature scattering.

Energetic electrons within IBs have isotropic pitch angle distributions, because curvature scattering by the magnetotail current sheet is always operating at strong diffusion limit (Sergeev et al., 2012, 2015). Specifically, the scattering rate depends exponentially on electron energy (Birmingham, 1984; Büchner & Zelenyi, 1989), leading to a sharp transition between strong diffusion and no precipitation (see Artemyev, Orlova, et al., 2013; Young et al., 2008, for variations in curvature scattering diffusion rate with electron energy). In other words, curvature scattering is unlikely to cause *weak* precipitation. Hence, monitoring electron precipitation within IBs does not require measurements of the full pitch angle distribution. Alternatively, locally-trapped electrons that are outside the bounce loss cone can also reflect the properties of IBs, provided that such IB regions can be identified and distinguished from other precipitation patterns. This feature enables the utilization of the high-energy-resolution CIRBE (Li et al., 2024) measurements for investigating electron IBs, in addition to the primary mission goal of studying the inner belt electrons which leads to the design focus of CIRBE on measuring the locally-trapped electrons with energies above 250 keV (Li et al., 2022). However, before utilizing CIRBE measurements for in-depth analysis of electron IBs, it is necessary to establish a robust method for identifying electron IBs using locally-trapped fluxes.

Since CIRBE/REPTile-2 measures electrons with energies above 250 keV, two issues must be addressed before utilizing the CIRBE data set for routine investigations of electron IBs: (a) identifying distinguishing characteristics for the high-energy part of IBs in the absence of measurements for typical plasma sheet electrons (<200keV, see Artemyev, Angelopoulos, et al., 2022); (b) discerning between electron precipitations within IBs and relativistic electron precipitation induced by EMIC waves (see examples of such nightside precipitation patterns in Artemyev et al., 2023; Capannolo et al., 2019; Capannolo, Li, Millan, et al., 2022). The second issue is especially important for periods of substorm injections that transport plasma sheet ions into the inner magnetosphere and drive EMIC waves in the premidnight sector (H. Chen et al., 2020; Jun et al., 2019, 2021). Such EMIC waves can effectively scatter the relativistic electrons right equatorward of the electron IB and cause relativistic electron precipitations (e.g., Artemyev et al., 2023; Capannolo et al., 2023), making the identification of IBs complicated. Statistical analysis of POES measured relativistic electron precipitations in the nightside sector has found multiple overlaps of EMIC-driven and curvature scattering precipitation patterns (see discussion in Capannolo, Li, Millan, et al., 2022; Yahnin et al., 2017). Moreover, some EMIC-driven precipitation events even exhibit energy-latitude dispersion (Grach et al., 2024), which is usually associated with curvature scattering (see Wilkins et al., 2023, and references therein), adding more difficulty in the separation between IBs and EMIC-driven precipitations.

This study aims to tackle two aforementioned challenges in IB identification using CIRBE measurements. Firstly, we utilize ELFIN electron measurements of both precipitating and locally-trapped fluxes to delineate the IB features expected in CIRBE measurements. Secondly, we combine CIRBE and POES measurements to elucidate the similarity and differences in electron precipitations due to IBs and EMIC waves. We present a detailed analysis of electron measurements from four nightside crossings of the CIRBE CubeSat during a substorm event on 22 Jun 2023. Finally, we discuss possible mechanisms that are responsible for the observed electron precipitation on the nightside, including whistler-mode waves, curvature scattering and EMIC waves. Our cross-analysis of the CIRBE, POES, and ELFIN data sets confirms that the high-energy-resolution CIRBE data can be utilized for investigating the dynamics of energetic electrons in the near-Earth magnetotail and plasma sheet region. In particular, our findings demonstrate that CIRBE measurements can reveal the fine energy dispersion in electron IBs with locally-trapped flux only, indicating that the effect of electron curvature scattering, the primary mechanism of electron loss in the transition region between magnetotail and radiation belt, can be identified by the locally-trapped electron measurements at low altitudes. This result suggests that curvature scattering effectively changes the anisotropy in electron flux within this region, and that it is necessary to include this effect in the modeling of radiation belt dynamics.

2. Data Set Description

CIRBE is a 3U CubeSat recently launched into a sun-synchronous orbit with 97.4° inclination and 509 km altitude (Li et al., 2022, 2024). The sole scientific instrument onboard is the Relativistic Electron and Proton Telescope integrated little experiment-2 (REPTile-2) (Khoo et al., 2022). REPTile-2 inherited the design of REPTile on CSSWE (Li et al., 2012, 2013, 2017; Li, 2024; Schiller et al., 2014; K. Zhang et al., 2017), with an improved time resolution of 1 s and finer energy resolution. REPTile-2 measures 0.25–6 MeV electrons with 60 channels and 6.5–100 MeV protons with 60 channels. Khoo et al. (2022) provides a comprehensive description of the simulated response of REPTile-2's energy channels to incident particles with different energies. In this paper, we are using the incident energy based on the bowtie analysis as the particle's energy in each channel and thus the lowest energy channel of electron is considered as 300 keV (see Khoo et al., 2022, for details). REPTile-2 has a field-of-view of 51° and a look direction of nearly perpendicular to the background magnetic field, therefore, REPTile-2 measures perpendicular/90° fluxes, which are generally locally-trapped fluxes except in some particular regions such as the northern conjugate of the South Atlantic Anomaly (SAA) region (K. Zhang et al., 2020).

Electron Losses and Fields Investigation (ELFIN) consists of two identical CubeSats and were launched into a polar orbit with 93° inclination and 450 km altitude in 2018 (Angelopoulos et al., 2020). The Energetic Particle Detector (EPD) onboard ELFIN provides electron measurements from 50 keV to 7 MeV with 16 channels and resolves the pitch angle in 16 sectors. Therefore, ELFIN can measure the locally-trapped fluxes and precipitating fluxes separately (e.g., X.-J. Zhang et al., 2022).

In this study, ELFIN measurements will be used to reveal the morphology of electron IB and EMIC-driven precipitation as appeared in locally-trapped fluxes. Then we will present the nightside electron measurements from 300 keV to 2 MeV by CIRBE during a substorm event in 22 Jun 2023. Figure 1a shows the profile of AE index determined using THEMIS ground stations during this event. The vertical dashed lines mark the time of the four CIRBE passes that will be discussed in this study. The orbit of CIRBE is mapped to the magnetic equator and displayed in Figure 1b as the gray solid curves. The radial distance represents L value and the polar angle represents magnetic local time (MLT), both calculated under the IGRF model (Thébault et al., 2015). The four passes used in this study is highlighted with color as noted in the figure. In addition, several other satellites are used as supportive observations, including NOAA/POES satellites (Yando et al., 2011), GOES-18 (Boudouridis et al., 2020) and KOMPSAT (Constantinescu et al., 2020; Magnes et al., 2020). The locations of these satellites are also marked in Figure 1b.

3. Observations

3.1. ELFIN: Electron Isotropy Boundary and EMIC-Driven Precipitations

Figure 2 shows three examples of ELFIN crossings in the nightside, measuring the low-altitude projection of the inner magnetosphere and plasma sheet. The first two examples of ELFIN observations are displayed in Panels (a–h), presenting two electron IB events identified using the combination of locally-trapped and precipitating electron fluxes. The main characteristics of IB appeared in locally-trapped electron flux will be inspected and used for

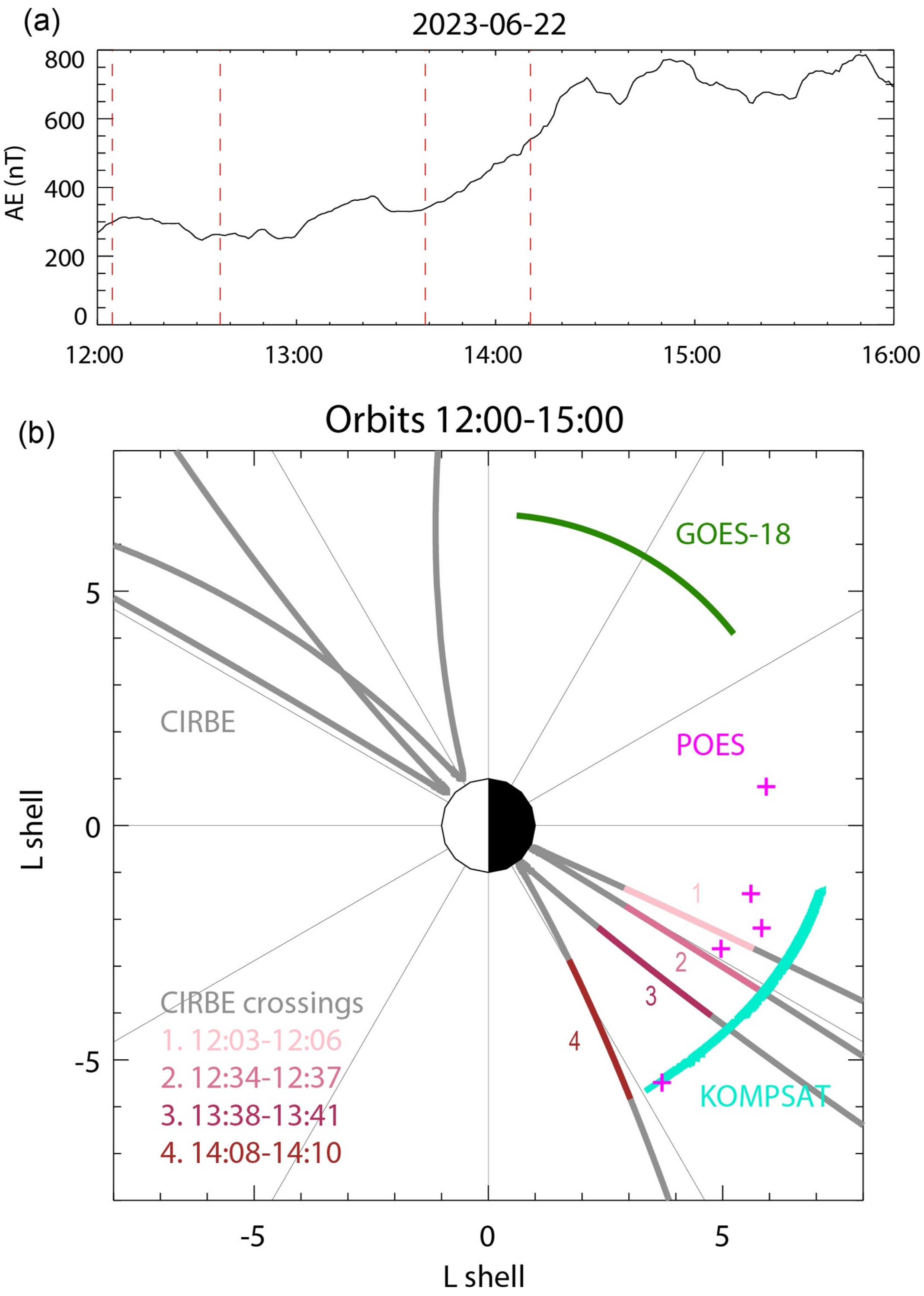

Figure 1. (a) The time profile of AE index in the substorm in 22 Jun 2023. Vertical dashed lines mark the time of four nightside crossings of CIRBE. (b) Orbits of CIRBE (gray), KOMPSAT (cyan) and GOES-18 (green) during the substorm event, mapped to the equatorial plane. The magenta crosses mark the location of the isotropy boundaries observed by POES satellites (see appendix for the event list). The four CIRBE crossings used in this study is color-coded with time as noted in the figure. The radial distance represents L and the polar angle represents MLT with noon to the left.

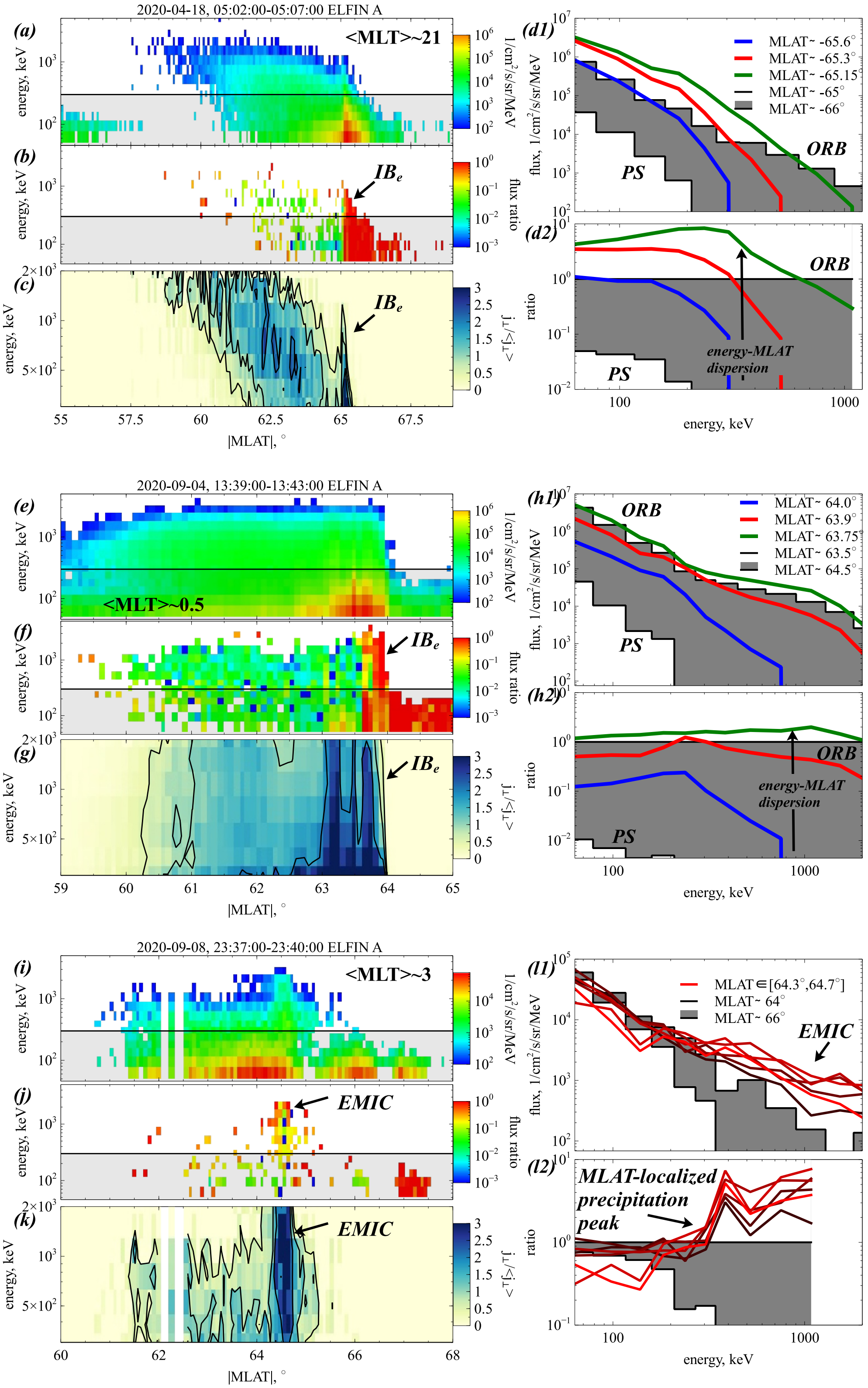
2020-04-18, 05:02:00-05:07:00 ELFIN A
(a)
<MLT>~21
(b)
IB$_e$
(c)
IB$_e$
energy, keV
1/cm^2/s/sr/MeV
flux ratio
j$_\perp$/<j$_\perp$>
|MLAT|, °
55 57.5 60 62.5 65 67.5
(d1)
MLAT~ -65.6°
MLAT~ -65.3°
MLAT~ -65.15°
MLAT~ -65°
MLAT~ -66°
ORB
PS
flux, 1/cm^2/s/sr/MeV
(d2)
ORB
energy-MLAT dispersion
PS
ratio
energy, keV
100 1000
2020-09-04, 13:39:00-13:43:00 ELFIN A
(e)
<MLT>~0.5
(f)
IB$_e$
(g)
IB$_e$
59 60 61 62 63 64 65
(h1)
ORB
MLAT~ 64.0°
MLAT~ 63.9°
MLAT~ 63.75°
MLAT~ 63.5°
MLAT~ 64.5°
PS
(h2)
ORB
energy-MLAT dispersion
PS
2020-09-08, 23:37:00-23:40:00 ELFIN A
(i)
<MLT>~3
(j)
EMIC
(k)
EMIC
60 62 64 66 68
(l1)
MLAT∈[64.3°,64.7°]
MLAT~ 64°
MLAT~ 66°
EMIC
(l2)
MLAT-localized precipitation peak

Figure 2.

identifying IBs in CIRBE measurements. Panels (a and b) show the profiles of both locally-trapped and precipitating electron fluxes of a quiet-time plasma sheet crossing, with an observed IB region that is relatively wide in latitude and expands from 65° to ~66° in the energy range of [50,1000] keV. The black horizontal line marks the lower energy limit of the CIRBE/REPTile-2 detector (250 keV), thus only the part above this line would be measured by CIRBE, which covers ~0.5° in latitude. Panel (c) shows the trapped fluxes normalized to the average trapped flux level for each energy channel, and these normalized fluxes highlight the IB region as a local enhancement. The local enhancement in trapped fluxes caused by IB can also been seen in Panel (a), however, it is significantly more obvious in the normalized trapped fluxes. Such enhancements of locally-trapped electron fluxes at low altitudes are typical for IB regions (e.g., Sergeev et al., 2012), because these electrons have small equatorial pitch angles despite being outside the bounce loss cone and can be enhanced by electron scattering in the near-equatorial region. This enhancement has a clear dispersive structure with the flux increase of higher energy electrons occurring at lower latitudes, which is a primary property of the curvature scattering mechanism in the magnetotail (see Sergeev et al., 1983).

Panel (d) displays the detailed energy spectrum evolution of the trapped flux enhancement to zoom in on the energy-latitude dispersion. The gray region is bounded by the flux levels at the latitude corresponding to the outer edge of the radiation belt, identified by $>100/\text{cm}^2/\text{s}/\text{sr}/\text{MeV}$ electron fluxes at ~1MeV (Mourenas et al., 2021), and the latitude corresponding to the plasma sheet, identified by the absence of $>100/\text{cm}^2/\text{s}/\text{sr}/\text{MeV}$ fluxes at above ~300keV (Artemyev, Angelopoulos, et al., 2022), marking the expected variation of electron energy spectrum between the plasma sheet and outer radiation belt. In other words, in absence of any IB-related enhancements, all spectra in this transition region should fall inside the gray region. Three colored curves show locally-trapped spectra measured in the transition region, with blue, red and green curves moving from the plasma sheet to the outer radiation belt. The blue line shows a large increase of <200keV fluxes relative to the plasma sheet flux level, then red curve shows <350keV fluxes exceeding both plasma sheet and outer radiation belt levels, and finally green curve shows <600keV fluxes exceeding plasma sheet and outer radiation belt levels. These dispersive and strong flux enhancements are more evident in panel (d2), where the same spectra are shown with the normalization to the outer radiation belt spectrum, that is, the upper boundary of the gray region from panel (d1). Such normalized fluxes reveal consecutive flux enhancements within IB, which can be used to identify the IB structures in the measurements of locally-trapped fluxes.

The main properties of the quiet-time IB from Figures 2a–2d are repeated in panels (e–h) which present an IB event observed by ELFIN during the substorm growth phase, when the reconfiguration of the magnetotail magnetic field lines results in the shrinking of the low-altitude projection of the near-Earth plasma sheet to a few degrees (Artemyev, Angelopoulos, et al., 2022). The transition region between the plasma sheet and outer radiation belt in this event is observed to be less than 0.5° in magnetic latitude, with a sharp increase of electron isotropic flux from the plasma sheet energies ~100 keV to the radiation belt energies ~3 MeV (see panel (f); [63.7°, 64°] latitudinal range). Thus, the normalized trapped fluxes exhibit strong energy-dispersionless boundary between plasma sheet and the outer radiation belt, that is, IB (see panel g). Comparison of panels (d1 and h1) shows similarity in the transition of trapped electron spectrum within the IB region: flux enhancements extend to higher energies moving equatorward and may exceed the radiation belt flux level. Although this energy-latitude dispersion is less evident for the sharp IB in panel (h1), the normalized spectra in panel (h2) clearly exhibit this dispersion: the normalized flux peaks at higher energy as magnetic latitude decreases (the blue and red curves representing energy spectra at higher latitude peak at ~250 keV while the green curve showing energy spectrum at lower latitude peaks at ~1 MeV). Note that panel (g) shows several energy-dispersionless peaks equatorward from the IB. These peaks are not only associated with the trapped flux increase, but also to the increase of precipitating-to-trapped flux ratio (see panel f). Such peaks are likely due to equatorial electron scattering by intense whistler-

Figure 2. Three examples of ELFIN observations of the nightside relativistic electron precipitation. Panels (a, e, i) show locally-trapped electron spectra. Panels (b, f, j) show precipitating-to-trapped flux ratio. Panels (c, g, k) show locally-trapped electron spectra normalized to the averaged flux of each energy channel. The black lines in these panels mark the lower energy limit of CIRBE measurements. Panels (d1, h1, l1) show line plots of the trapped electron spectra measured during the precipitation events. Panels (d2, h2, l2) show curves from panels (d1, h1, l1) normalized to the upper boundary of the gray region (outer radiation belt flux level for d1 and h1 and upper flux limit of the non-precipitating region for l1). In panels (d1, 2 and h1, 2), the gray regions represent the flux range between the plasma sheet and outer radiation belt for IB observations, whereas blue, red, and green curves show three spectra within the IB region. In panels (l1, 2) the gray region represent the typical energy spectra before and after EMIC-driven precipitation event, whereas red curves show electron spectra within EMIC-driven precipitation (with red color becoming darker as latitude decreases).

mode waves (see examples of such relativistic precipitations driven by whistler-mode waves around IB in Artemyev et al., 2024). In this event, the flux peak at ~63.75° overlaps with the IB, suggesting that whistler-driven electron scattering may also contribute to flux enhancement within IB.

Figures 2i–2l illustrates the ELFIN observations of EMIC-driven electron precipitation. There is a clear low-energy cut-off of the precipitating flux burst at around ~64.5° in magnetic latitude as shown in panel (j): the precipitating-to-trapped flux ratio has a maximum around 1 MeV and almost drops to zero as the energy decreases to 300 keV. Such cut-off is associated with the minimum energy of electrons resonating with EMIC waves (Summers & Thorne, 2003), and has been reported in multiple EMIC events observed by ELFIN (see Angelopoulos et al., 2023). Higher equatorial pitch angles require higher resonant energy, thus the energy cut-off is not observed in locally-trapped electron fluxes (Figure 2i). Note that the enhancement in locally-trapped electrons is driven by the same mechanism of resonant electron scattering by EMIC waves from larger pitch angles toward the loss cone (R. Shi et al., 2016), as electron flux typically peaks at 90° pitch angle. The normalized trapped fluxes exhibit latitudinal localized flux enhancement at ~64.5° in magnetic latitude (Figure 2k), which may be mixed with the similar enhancement at the sharp IB such as in panel (g). The major distinction of the EMIC-driven precipitation events from the sharp IB events is the absence of the energy-latitude dispersion in trapped fluxes. Comparison of panels (d1, 2 h1, 2 and l1, 2) demonstrates that EMIC-driven precipitations are characterized by electron flux enhancements without the transition from low energy enhancement at higher latitudes to the high energy enhancement at lower latitudes, which is typical for IB events. Note that EMIC waves could cause electron precipitations with energy-latitude dispersion as reported by ELFIN measurements (see Artemyev et al., 2023; Grach et al., 2024); however, these dispersive precipitations are observed at much lower magnetic latitudes compared to the IB locations in these events. To conclude, Figure 2 provides a simple receipt for the separation of these two types of nightside relativistic electron precipitation events, namely IB and EMIC-driven precipitation, with locally-trapped fluxes: inspection of the energy-latitude dispersion provides sufficient evidence for the identification of IB and EMIC-driven electron precipitations.

3.2. CIRBE: Electron Isotropy Boundary and EMIC-Driven Precipitations

With the characteristics of IB and EMIC-driven precipitations derived by the ELFIN measurements, we examine the time profile of the locally-trapped electrons observed by CIRBE during the 22 Jun 2023 substorm. CIRBE traverses the nightside magnetosphere twice before the substorm onset, roughly at 12:03–12:07 and 12:33–12:37, respectively. Electron measurements by CIRBE are shown in Figure 3 for the first pass and in Figure 4 for the second pass. CIRBE was located at around 22.5 in MLT in the first pass, and the original measured electron intensity is presented in Figure 3b. Due to its energy range, the high energy radiation belt electrons are the dominant population observed in the CIRBE passes. As magnetic latitude increases, the intensity of the core outer belt population, measured by CIRBE, rapidly decreases, along with the fading of >1 MeV electrons (fluxes fall below 1,000/cm^2/s/sr/MeV), marking the transition of the spacecraft location from the outer radiation belt to the plasma sheet. CIRBE observes an increase in the locally-trapped electron flux near the outer boundary of the outer belt, at about 61.8° in magnetic latitude. By comparing with the IB characteristics obtained by ELFIN in Figure 2a, such local flux increase in that particular region suggests that an IB is likely detected. In Figure 3c which presents the normalized trapped flux in the same style as (Figures 2c, 2g, and 2k), the IB feature can be seen more clearly. Furthermore, we inspect the locally-trapped and precipitating flux measured by the nearby MetOp-1 (one of the POES satellites) and show that precipitating electron fluxes (black dashed line) increase to match the trapped electron flux (black solid line) at around 61.5° (Figure 3a), validating that the observed flux enhancement in CIRBE is indeed electron IB. Note that Metop-1 also observes the proton IB, shown by the matching fluxes of the trapped protons (solid blue line) and precipitating protons (dashed blue line), right below (at a lower magnetic latitude of) the electron IB, and this is an expected feature of the electron and proton IBs. Similar features of electron IB are observed by CIRBE again in the second pass as shown in (Figures 4b and 4c), only at a slightly different magnetic latitude of −62.8°. The different magnetic latitude of the observed IB compared to the first pass is likely due to the different spatial locations of the measurements, such as the different hemisphere and MLT, rather than a real drastic change in the IB locations. The measurements of IBs by nearby NOAA-18 satellite is also shown in Figure 4a.

In general, the nightside electron precipitation observed in the form of IBs in the first two passes of CIRBE displays consistent patterns, as these two passes are both in the quiet time or the early growth phase of the substorm (Figure 1a). The panels d of both Figures 3 and 4 confirm dispersive pattern from Figures 2d2 and 2h2:

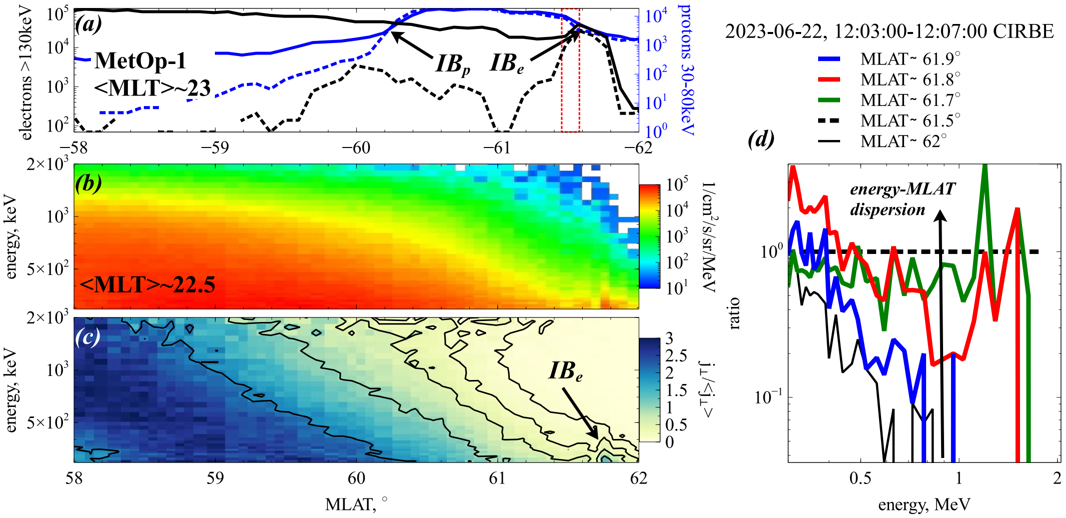

Figure 3. Electron observations in the first pass of CIRBE at 12:03–12:07. (a) >130 keV electron (black) and 30–80 keV proton (blue) fluxes measured by the nearby MetOp-1 satellite. Precipitating flux is plotted in dashed lines and locally-trapped flux is plotted in solid lines. (b) Energy-resolved locally-trapped electron fluxes measured by CIRBE as a function of magnetic latitude. (c) Locally-trapped electron fluxes normalized to the average flux in each channel as measured by CIRBE, similar to how ELFIN data is portrayed in Figures 2c, 2g, and 2k. (d) Energy spectra of the locally-trapped electrons at different magnetic latitudes normalized to the spectrum of the outer radiation belt electrons right equatorward of the observed IB (at the latitude of the dashed line). The blue, red and green lines represent locations from the plasma sheet to the outer radiation belt, while the black solid line shows the flux of the plasma sheet, similar to Figures 2d2 and 2h2.

the electron energy spectra become harder (relatively more increase in flux for high energy electrons) as CIRBE moves from high magnetic latitude to low magnetic latitude with a significant enhancement at >800 keV in the green line or the lowest magnetic latitude, exceeding the outer radiation belt flux level. In Figure 4d, it is also evident that, for <500 keV electrons, the fluxes increase as the CubeSat moves poleward, largely exceeding the plasma sheet flux level with those at middle and high latitude exceeding the outer radiation belt level. The clearly observed energy dispersion is resolved for the first time by the high energy resolution of REPTile-2 on CIRBE and emphasizes that the measured electrons in this region are dominated by curvature scattering within the current sheet, confirming the detection of IBs.

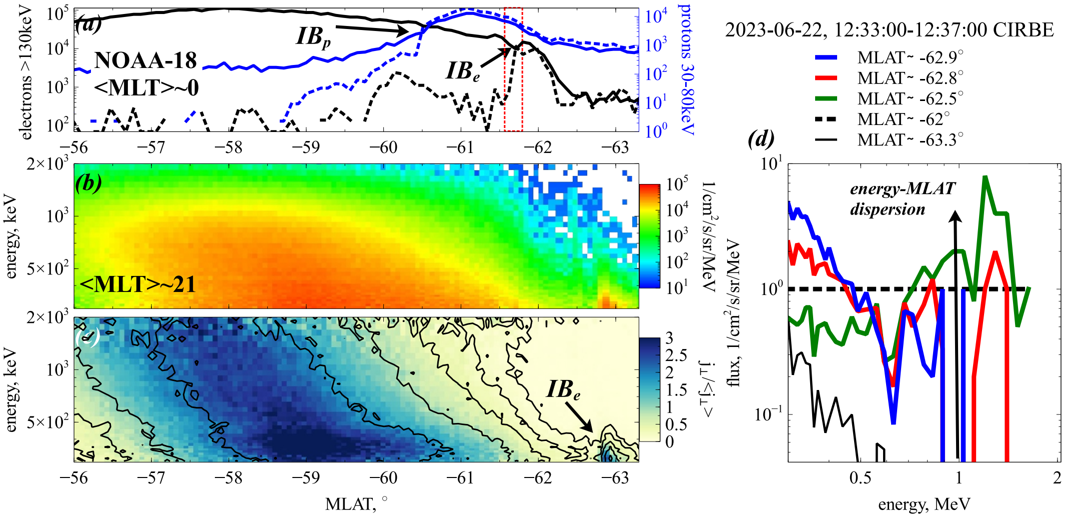

Figure 4. Electron observations in the second pass of CIRBE at 12:33–12:37, together with measurements by the nearly NOAA-18 satellite, in the same format as Figure 3.

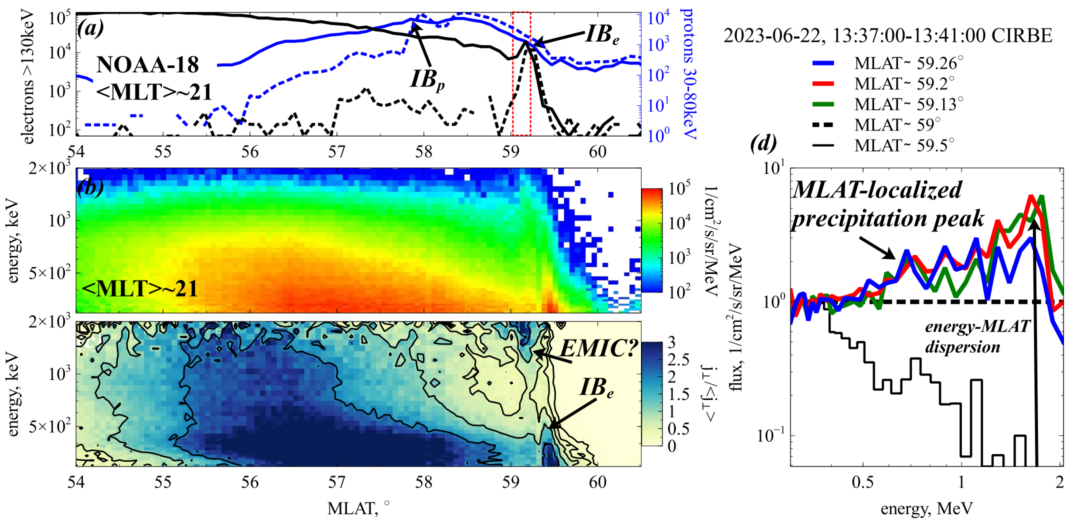

Figure 5. Electron observations in the third pass of CIRBE at 13:37–13:41, together with measurements by the nearly NOAA-18 satellite, in the same format as Figures 3 and 4.

One interesting feature observed by CIRBE is that there is a local flux minimum between the outer belt and IB for <0.6 MeV electrons in both Figures 3b and 4b, which is also present in ELFIN measurements in Figure 2a for ~0.3–0.6 MeV electrons. This feature can be commonly seen in previous ELFIN observations (e.g., Artemyev, Angelopoulos, et al., 2022; Wilkins et al., 2023). Such latitudinally localized flux minimum can be explained by the interplay of two trends of equatorial flux: (a) the flux increase with decreasing L-shell and (b) the increase of flux anisotropy with decreasing L-shell (due to the decrease in efficiency of curvature scattering in stronger magnetic field). The first trend should cause the flux to increase as the magnetic latitude decreases at low Earth orbit, assuming a constant flux anisotropy. The second trend should cause the flux to decrease as the magnetic latitude decreases, assuming a constant equatorial flux. For relativistic electrons (~1 MeV), the first trend is dominant due to the more isotropic fluxes and the very strong radial gradient across different L-shells in equatorial flux (no relativistic electron fluxes in the plasma sheet). However, for sub-relativistic electrons, the second trend may be strong enough to provide a local flux minimum at low altitudes, between the outer radiation belt and the IB region. By comparing the low-altitude and equatorial fluxes, Artemyev, Angelopoulos et al. (2022) shows that 50–500 keV electrons are indeed isotropic in the plasma sheet, whereas electrons at the same energies are highly anisotropic in the inner magnetosphere (e.g., R. Shi et al., 2016; Zhao et al., 2018). These observational results support that the second trend is expected to have a strong influence on the overall flux profile of sub-relativistic electrons measured at low altitudes.

Figure 5 shows the same analysis for the third pass of CIRBE, which is after the substorm onsite (Figure 1a). As CIRBE moves poleward, it first observes an enhancement primarily at high energy (>800 keV) and then encounters a sharp increase at low energy (<700 keV) (Figure 5b). Figure 5c further highlights the two enhancements centered at upper energy limit and the lower energy limit of this plot, respectively. On one hand, the enhancement at low energy exhibit similar patterns as the September 4 2020 event observed by ELFIN (Figures 2f and 2g): the increase is sharp and extends to higher energy than quiet time, suggesting the presence of an IB during/after substorm growth phase. The nearby NOAA-18 satellite also confirms the existence of the electron IB at a similar magnetic latitude (Figure 5a). On the other hand, the enhancement at high energy is likely the result of the combination of two scattering mechanisms. This enhancement is more concentrated above ~ 1 MeV, suggesting increased precipitation of relativistic electrons that is usually associated with EMIC wave activities. However, in Figure 5d, the detailed normalized energy spectra of this enhancement show a pattern that is consistent with the curvature scattering mechanism. In particular, 1 MeV electrons have highest fluxes at higher magnetic latitude (blue line, 59.26° in magnetic latitude) and with increasing energy, highest fluxes are observed in the red line at 59.2° latitude and then in the green line at 59.13° latitude. Therefore, the dispersed energy spectra at different magnetic latitudes indicate that curvature scattering plays an important role in causing the enhanced MeV electron fluxes at low altitudes that suggests enhanced precipitation in the third CIRBE pass. It is worth noting that the energy dispersion is much less obvious compared to the clear IB events in the first two passes,

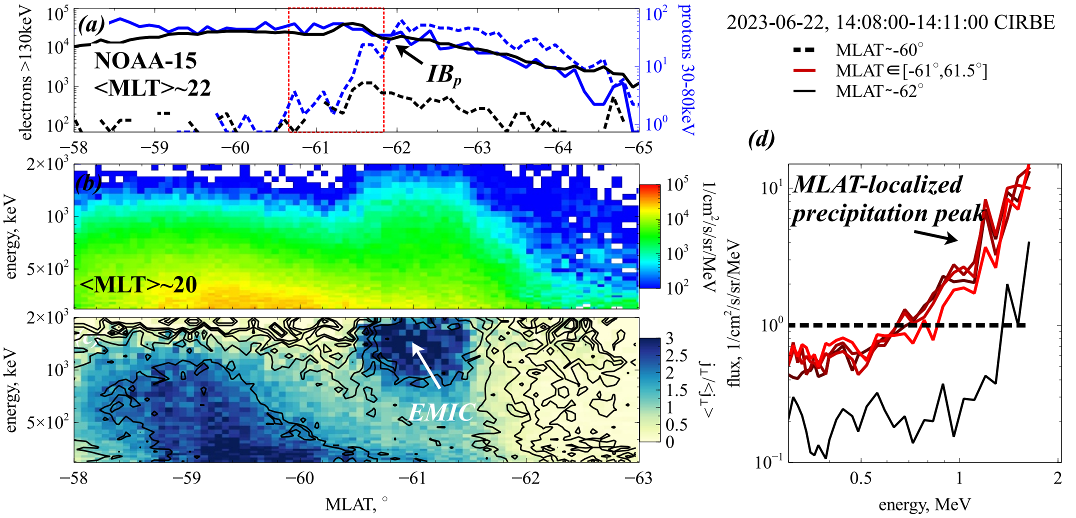

Figure 6. Electron observations in the fourth pass of CIRBE at 14:08–14:11, together with measurements by the nearby NOAA-15 satellite. Panels (a–c) are in the same format as in Figures 3–5. (d) Electron energy spectra in the precipitation region (red) normalized to the outer radiation belt flux level outside of the precipitation region at the latitude indicated by the black dashed line (with red color becoming darker as latitude decreases). Black solid line and black dashed line represent electron energy spectra right out of the region with local flux enhancement seen in panel (c).

suggesting that contributions from other mechanisms such as the EMIC waves may be equally important during this CIRBE pass. Indeed, overlaps between IB and EMIC-driven precipitation are commonly observed in the nightside magnetosphere (see Artemyev et al., 2023; Capannolo, Li, Millan, et al., 2022). With its high energy resolution, CIRBE may be able to detect the fine structures in the electron energy spectrum and help distinguish between the dispersive (presumably due to IB) and the dispersionless (presumably due to EMIC) precipitation patterns, however, distinguishing between these two types of events may still be difficult in specific cases.

The fourth pass of CIRBE is further away from the midnight and thus has likely moved out of the zone where IBs can be observed (Figure 1). Instead, CIRBE observes a very typical EMIC-driven electron precipitation, featuring a lower energy limit in the precipitating fluxes (Figure 6). In contrast with the third pass, CIRBE only observes clear enhancement in electrons with energies greater than 600 keV, and no substantial enhancement is seen at lower energies. Figure 6d shows the detailed normalized energy spectra of the electrons in the precipitation region (red lines) in comparison with the flux level outside the precipitation region (black dashed line). It is evident that electrons in the precipitation region have relatively lower fluxes at energies below 600 keV and much higher fluxes in the MeV range compared to the normal level indicated by the black dashed line. This low-energy cut-off feature resembles the measurement of ELFIN shown in Figures 2i–2l, and is a clear indicator of the EMIC wave driver, due to the minimum resonate energy in electrons that can be scattered by the EMIC waves. Note that this event is observed near the isotropy boundary of 30–80 keV protons (see Figure 6a), so we cannot use proton precipitation measurements to confirm the equatorial EMIC source region. However, for EMIC-driven electron precipitations at lower L-shell, analysis of concurrent proton precipitations by low-altitude satellites such as POES can help confirm the EMIC wave activities (e.g., Carson et al., 2013; Miyoshi et al., 2008).

Even though there is no direct evidence of EMIC wave activity found during this time, measurements from GOES-18 and KOMPSAT confirm that injection has happened prior to the observed enhanced electron precipitation. Figure 7 shows that GOES-18 detects the electron injection at around 14:00 in the post-midnight sector and KOMPSAT observes low frequency waves in magnetic field measurements that also indicate injection starting at around 13:40 in pre-midnight sector near CIRBE. The injected plasma sheet protons can serve as an energy source for the generation of EMIC waves, which typically drive the enhanced precipitation of high energy (>600 keV) electrons. However, due to the localized nature of EMIC waves, their presence and connection to the observed electron precipitation cannot be confirmed through in situ wave measurements in this event. The nearby NOAA-15 satellite shows that the magnetic latitude of the electron precipitation region is right below the proton IB (Figure 6a), ruling out the possibility of curvature scattering as the cause for the enhanced electron precipitation, because the electron IB is supposed to be more poleward than the proton IB. Since the observed electron

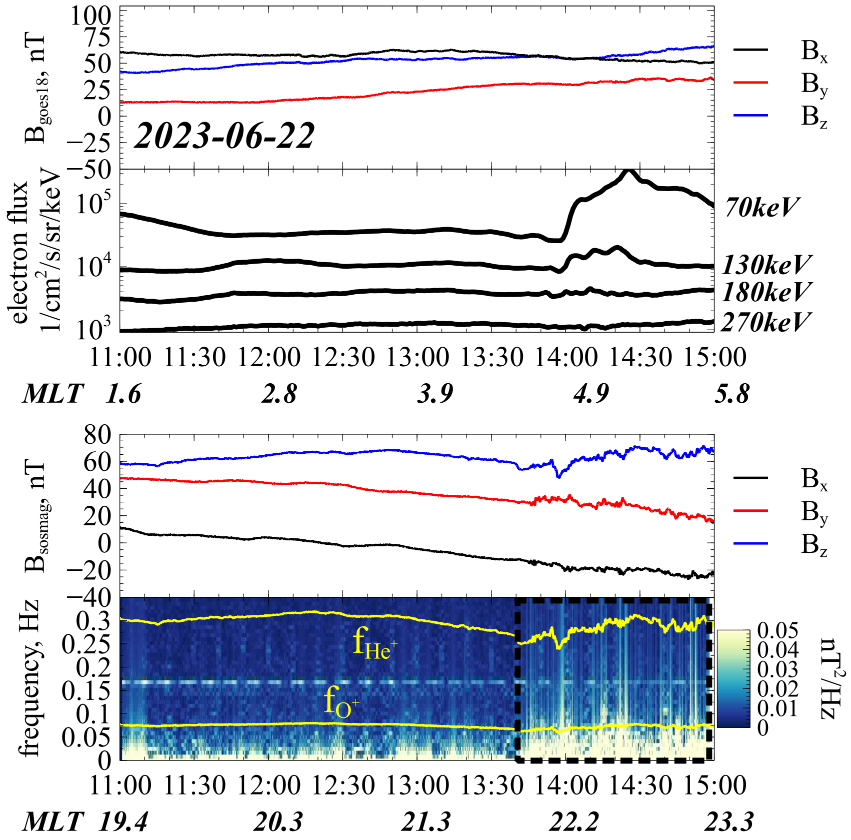

Figure 7. (a) Magnetic field components measured by GOES-18 in GSM coordinate. (b) Electron fluxes measured by GOES-18 satellites at 70, 130, 180 and 270 keV. (c) Magnetic field measured by KOMPSAT in GSM coordinate. (d) Power spectrogram in the frequency range of 0–0.4 Hz measured by KOMPSAT. Yellow lines mark the gyrofrequencies of He^+ and O^+, black box shows the interval with wave activity.

precipitation by CIRBE is unlikely to be associated with electron IB, EMIC wave is the most likely driver considering that the energy of the precipitating electrons extends to well above MeV.

4. Discussion of Potential Nightside Electron Precipitation Mechanisms: Isotropy Boundary, EMIC-Driven, and Whistler-Driven Precipitations

In this paper, we utilize the nightside relativistic electron precipitations measured by ELFIN to investigate the different patterns of isotropy boundary and EMIC-driven precipitations, in order to establish a reliable method for discerning these two types of precipitations with locally-trapped fluxes only. We found that the key to differentiate IBs and EMIC-driven precipitations is the energy-latitude dispersion of the enhanced electron fluxes. However, this method requires that no other possible precipitation mechanisms are present during the specific event. Near-Earth plasma sheet electrons rarely exhibit a significant relativistic population (>0.5MeV), except in cases of the most intense acceleration events (e.g., Artemyev, Hoshino, et al., 2013; Cohen et al., 2021; Eriksson et al., 2020; Turner et al., 2021). The enhancements of these relativistic fluxes at low altitudes often signal the transition region between the outer radiation belt and the plasma sheet (Artemyev, Angelopoulos, et al., 2022). Therefore, the precipitation of relativistic electrons can be attributed either to curvature scattering within such transition regions (Wilkins et al., 2023) or to wave-particle resonant interactions within the outer radiation belt. Two primary wave modes are potentially capable of driving relativistic electron precipitation: whistler-mode waves and EMIC waves (Thorne et al., 2021). We will first eliminate whistler-mode waves as potential drivers of observed precipitation patterns and subsequently explore the roles of EMIC waves and curvature scattering.

Nightside precipitation induced by whistler-mode waves is typically limited to sub-relativistic energies due to the latitudinal localization of whistler intensity (Agapitov et al., 2013). The most intense field-aligned waves (Agapitov, Mourenas, Artemyev, Mozer, Hospodarsky, et al., 2018; Li et al., 2011) scatter electrons below

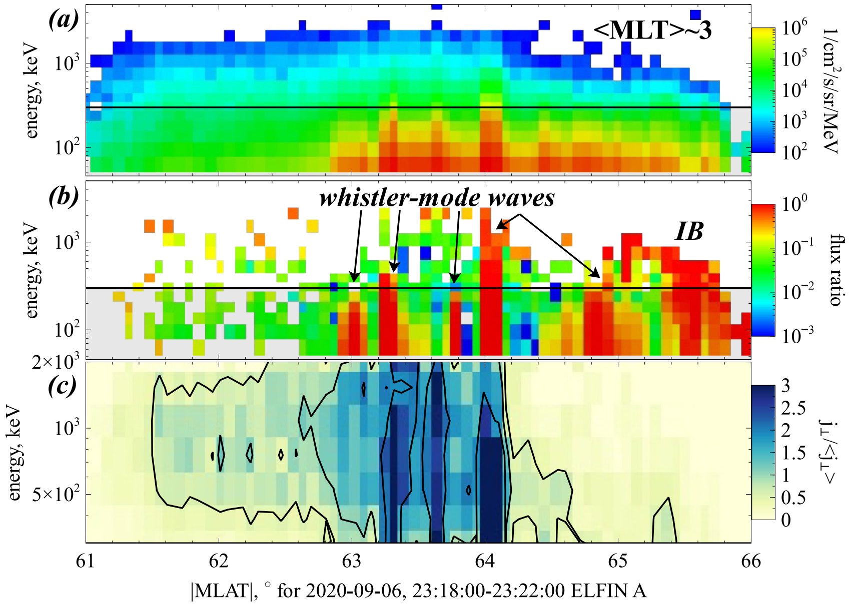

Figure 8. The example of ELFIN observations of the nightside relativistic electron precipitation driven by whistler-mode waves. Panel (a) shows locally-trapped electron spectra. Panel (b) shows precipitating-to-trapped flux ratio. Panel (c) shows locally-trapped electron spectra normalized to the averaged flux of each energy channel. The black horizontal lines mark the lower energy limit of CIRBE measurements.

100 keV at the equator (e.g., Li et al., 2013). The scattering of electrons at 0.5 MeV would require wave propagation along the field line to middle magnetic latitudes, above 30° (Artemyev et al., 2021). Such propagation can be facilitated by wave ducting (L. Chen et al., 2022; R. Chen et al., 2021; Ke et al., 2021), resulting in relativistic electron precipitation observed at low altitudes during plasma injections (Tsai et al., 2022, 2023). However, the source regions of whistler-mode waves are localized across magnetic field lines (Agapitov et al., 2017; Agapitov, Mourenas, Artemyev, Mozer, Bonnell, et al., 2018), causing bursty precipitations with intense flux enhancements confined to a latitudinal range of 0.1° to 0.5° (Artemyev et al., 2024). Figure 8 presents an example of relativistic electron precipitation associated with whistler-mode waves measured by ELFIN. The bursty feature of the precipitations and absence of low-energy cut-off as shown in the original and normalized locally-trapped fluxes in panels (a and c) suggest that this is a different type of precipitation than the events shown in the previous sections of this paper. It is worth noting that investigating such bursty precipitations solely with trapped flux measurements would necessitate the development of an identification procedure, which is beyond the scope of this study. Compared with Figures 2 and 8 suggests that IB and EMIC-driven precipitation events are of a larger scale and distinguishable from the bursty precipitations caused by whistler-mode waves.

Therefore, this study focuses on the separation between IB and EMIC-driven precipitations with flux measurements of the locally-trapped electrons. Using the dispersive feature of IB related precipitations, we are able to distinguish between these two types of precipitation patterns, paving the way for the statistical analysis of these two types of precipitations using the high energy resolution data set from the CIRBE CubeSat. However, under rare conditions this method may fail to distinguish between IB and EMIC-driven precipitation. The energy-latitude dispersion of IB events is caused by the electron curvature scattering in the magnetotail current sheet, where the scattering rate exponentially scales with the electron adiabatic parameter, $\propto \exp\left(-C\kappa^2\right)$ with $\kappa^2 = R_c/\rho_e$. R_c is the curvature radius of the field lines in the current sheet and $R_c \approx cB_{eq}/4\pi j_y$, where j_y is the current density and B_{eq} is the equatorial magnetic field. $\rho_e = m_e c^2\sqrt{\gamma^2 - 1}/eB_{eq}$ is the relativistic (γ is the Lorentz factor) electron (with mass m_e, charge $-e$) gyroradius (see models in Artemyev et al., 2015; Büchner & Zelenyi, 1989). Therefore, the scattering rate is a function of $B_{eq}^2/\sqrt{\gamma^2 - 1}$, leading to the dispersed precipitation from the near-Earth plasma sheet with strong radial gradient of the equatorial field B_{eq} (Dubyagin et al., 2002; Sergeev et al., 1983, 2012, 2023). Some EMIC-driven electron precipitations also exhibit energy-latitude dispersion (e.g., Artemyev et al., 2023; Grach et al., 2024), due to the dependence of the minimum resonant energy on plasma density, N_{eq}, and magnetic field: $\gamma_{EMIC} \propto B_{eq}/\sqrt{N_{eq}}$ (Summers & Thorne, 2003). For a dipole magnetic field, $B_{eq} \propto L^{-3}$, and empirical plasma density model with $N_{eq} \propto L^{-4}$ (Sheeley et al., 2001), we obtain following scalings for moderately relativistic electrons (1–3 MeV, $\gamma \in [3,7]$): $\gamma_{IB} \propto B_{eq}^2 \propto L^{-6}$ and $\gamma_{EMIC} \propto B_{eq}/\sqrt{N_{eq}} \propto L^{-1}$ (for sub-relativistic electrons $\gamma_{IB} \propto B_{eq}^4 \propto L^{-12}$). These dependences can be modified by the current density j_y and EMIC wave frequency variations with L: for example, one can get $\gamma_{EMIC} \propto B_{eq}^2/\sqrt{N_{eq}} \propto L^{-4}$ for low frequency EMIC waves (see Grach et al., 2024), whereas earthward gradient of $j_y \propto 1/L$ may provide $\gamma_{IB} \propto B_{eq}^2/j_y \propto L^{-5}$ (see $j_y(L)$ profile in Sitnov et al., 2019; Stephens et al., 2019; Sergeev et al., 2023). Therefore, in extreme situations, the energy-latitude dispersion can be similar for IB and EMIC-driven precipitations. In these rare cases, discerning between these two types of precipitations is difficult even with electron measurements with fully resolved pitch-angle distributions (Artemyev et al., 2023).

Here we propose several useful approaches to resolve this issue in future statistical studies: (a) selecting events with both IB and equatorward EMIC-driven precipitation observed simultaneously (see supporting information of Artemyev et al., 2023), (b) considering EMIC-driven precipitations at lower L shells in the dusk flank, where IBs are less frequently observed (Wilkins et al., 2023), (c) selecting EMIC-driven precipitations with clear low-energy cut-off (Angelopoulos et al., 2023), which is not observed in IBs (Wilkins et al., 2023). For example, Figure 6 shows a typical EMIC-driven precipitation event with weak (almost no) energy-latitude dispersion and clear low-energy cut-off of in the enhanced fluxes (see panels c and d). In addition, combining CIRBE electron measurements and POES ion measurements can also help distinguish between IBs and EMIC-driven precipitations, as only EMIC-driven precipitations are possible equatorward from the ion IB with electron IBs always being poleward from ion IBs (e.g., Shekhar et al., 2017; Yahnin et al., 2016, 2017).

5. Summary and Outlook

In this study, we use the energy and pitch angle resolved energetic electron fluxes from ELFIN to develop the method for distinguishing between two major nightside patterns of relativistic electron precipitations: curvature scattering within the isotropy boundary region and electron resonant scattering by EMIC waves. Because these precipitation mechanisms operate in the strong diffusion limit, the observed locally-trapped flux and precipitating flux are close to identical, enabling the use of locally-trapped flux measurements in the investigation of electron precipitations. We examine the energy-latitude dispersion of electron precipitation events to separate electron curvature scattering from EMIC-driven precipitations solely based on locally-trapped flux measurements. We demonstrate that this method performs well on the new data set of the CIRBE CubeSat by presenting a substorm event in which IBs and EMIC-driven precipitations are both observed and successfully identified. In particular, thanks to the high energy resolution of REPTile-2, CIRBE reveals unprecedentedly clear energy-latitude dispersion of the electron precipitations caused by electron curvature scattering, serving as a decisive evidence in distinguishing them from EMIC-driven electron precipitations. The results of this study suggest that CIRBE measurements are suitable for the nightside statistics of relativistic electron precipitation events.

Finally, there are several outstanding scientific questions that can be addressed with future CIRBE statistics of IB and EMIC-driven precipitation patterns:

Small-scale structures of IB: Electron precipitations due to scattering by magnetic field line curvature are highly sensitive to even subtle variations in the equatorial magnetic field (e.g., X. Shi et al., 2024), making IB patterns a valuable tool for remotely monitoring near-Earth magnetotail dynamics (Dubyagin et al., 2002; Sergeev et al., 2012, 2018). The high energy resolution of CIRBE/REPTile-2 measurements offers a unique opportunity to investigate weak variations in electron fluxes attributable to equatorial magnetic field dynamics within the plasma injection region (Lin et al., 2014; Panov et al., 2019; Panov & Pritchett, 2018; Sorathia et al., 2020).

Low-energy cut-offs in EMIC-driven precipitations: The comparison between model predictions and observations reveals a systematic discrepancy, with theoretical models expecting a minimum resonant energy of ~1 MeV (Summers & Thorne, 2003; Silin et al., 2011; L. Chen et al., 2019; Grach & Demekhov, 2020), whereas observations show a sub-relativistic cut-off (e.g., An et al., 2022; Capannolo et al., 2019; Hendry et al., 2017; Nakamura et al., 2022). Although statistics obtained from ELFIN measurements have significantly advanced our understanding of these sub-relativistic precipitations (An et al., 2024; Angelopoulos et al., 2023), the finer energy resolution of CIRBE/REPTile-2 can offer more precise measurements of the loss of sub-relativistic electrons in

EMIC-driven precipitation events. Such information is crucial for comprehending the regimes of wave-particle resonant interactions (see discussion in Angelopoulos et al., 2023; Hanzelka et al., 2023; Grach & Demekhov, 2023).

Systematic differentiation of IBs and EMIC-driven precipitations: Nightside energetic electron precipitations by EMIC waves are often linked with ion injections from the plasma sheet (e.g., H. Chen et al., 2020; Jun et al., 2019, 2021), located just earthward from the inner magnetotail edge (e.g., Dubyagin et al., 2011; Sergeev et al., 2014), overlapping with the region where IBs are typically observed (Newell et al., 1998; Sergeev et al., 2012; Sivadas et al., 2019). Such spatial closeness of these IBs and EMIC-driven precipitations often complicates the distinction between these two precipitation patterns (see discussion in Artemyev et al., 2023; Capannolo, Li, & Huang, 2022; Shekhar et al., 2018; Yahnin et al., 2016), especially for the events during substorm growth phase, when IBs can move into the inner magnetopshere region due to the stretched magnetic field line (e.g., Murase et al., 2022; Zou et al., 2024). However, the high energy resolution of CIRBE/REPTile-2 measurements may help detect subtle variations in electron energy spectrum to statistically differentiate between the dispersive IB structures and the less dispersive EMIC-driven precipitation events.

Appendix A: List of IBs Observed by POES Satellites

Table A1 lists the locations and times of the observed IBs by POES satellites during the 22 Jun 2023 substorm. Figure 1 shows that the nightside flux enhancements observed by CIRBE are consistent with the region where IBs are observed by POES satellites, confirming that CIRBE successfully identifies the IBs with the locally-trapped electron measurements.

Table A1
IBs Observed by POES Satellites

Satellite	mlat (deg)	MLT (hrs)	Time (UT)
MetOp-1	−61.38	23.03	11:51
POES-18	−61.71	0.53	12:10
MetOp-3	−62.56	22.63	12:44
POES-18	59.07	20.27	12:47
MetOp-1	−61.71	22.14	13:34

Data Availability Statement

ELFIN data are publicly available at ELFIN data archive https://data.elfin.ucla.edu. CIRBE data are publicly available at https://lasp.colorado.edu/cirbe/data-products/. NOAA/POES and GOES data used in this study are publicly available at https://cdaweb.gsfc.nasa.gov. GEO-KOMPSAT-2A (SOSMAG) data are made available via ESA's Space Safety Programme and its provision forms part of the ESA Space Weather Service System at https://swe.ssa.esa.int. Data access and processing was done using SPEDAS V3.1, see Angelopoulos et al. (2019). The mapping of the satellite positions to geomagnetic coordinates is conducted using the International Radiation Belt Environment Modeling (IRBEM) library (v4.4.0), the latest version of which can be found at Boscher et al. (2022).

Acknowledgments
A. V. A., X. J.Z., and V. A. acknowledge support by NASA awards 80NSSC23K0108, 80NSSC23K0403, 80NSSC24K0558, and NSF grants AGS-1242918, AGS-2019950, and AGS-2021749. CIRBE mission is supported by NASA Grant 80NSSC19K0995. We acknowledge the GEO-KOMPSAT-2A magnetometer team for their high quality data set: Ulrich Auster, Dragos Constantinescu (Institut für Geophysik und Extraterrestrische Physik, Technische Universität Braunschweig, Braunschweig, Germany) and David Fischer, Werner Magnes (Space Research Institute, Austrian Academy of Sciences, Graz, Austria).

References

Agapitov, O. V., Artemyev, A., Krasnoselskikh, V., Khotyaintsev, Y. V., Mourenas, D., Breuillard, H., et al. (2013). Statistics of whistler mode waves in the outer radiation belt: Cluster STAFF-SA measurements. *Journal of Geophysical Research*, *118*(6), 3407–3420. https://doi.org/10.1002/jgra.50312

Agapitov, O. V., Blum, L. W., Mozer, F. S., Bonnell, J. W., & Wygant, J. (2017). Chorus whistler wave source scales as determined from multipoint Van Allen Probe measurements. *Geophysical Research Letters*, *44*(6), 2634–2642. https://doi.org/10.1002/2017GL072701

Agapitov, O. V., Mourenas, D., Artemyev, A., Mozer, F. S., Bonnell, J. W., Angelopoulos, V., et al. (2018). Spatial extent and temporal correlation of chorus and hiss: Statistical results from multipoint THEMIS observations. *Journal of Geophysical Research: Space Physics*, *123*(10), 8317–8330. https://doi.org/10.1029/2018JA025725

Agapitov, O. V., Mourenas, D., Artemyev, A. V., Mozer, F. S., Hospodarsky, G., Bonnell, J., & Krasnoselskikh, V. (2018). Synthetic empirical chorus wave model from combined Van Allen Probes and Cluster statistics. *Journal of Geophysical Research: Space Physics*, *123*(1), 297–314. https://doi.org/10.1002/2017JA024843

An, X., Artemyev, A., Angelopoulos, V., Zhang, X., Mourenas, D., & Bortnik, J. (2022). Nonresonant scattering of relativistic electrons by electromagnetic ion cyclotron waves in Earth's radiation belts. *Physical Review Letters*, *129*(13), 135101. https://doi.org/10.1103/PhysRevLett.129.135101

An, X., Artemyev, A., Angelopoulos, V., Zhang, X.-J., Mourenas, D., Bortnik, J., & Shi, X. (2024). Nonresonant scattering of energetic electrons by electromagnetic ion cyclotron waves: Spacecraft observations and theoretical framework. *Journal of Geophysical Research: Space Physics*, *129*(3), e2023JA031863. https://doi.org/10.1029/2023ja031863

Angelopoulos, V., Cruce, P., Drozdov, A., Grimes, E. W., Hatzigeorgiu, N., King, D. A., et al. (2019). The space physics environment data analysis System (SPEDAS). *Space Science Reviews*, *215*(1), 9. https://doi.org/10.1007/s11214-018-0576-4

Angelopoulos, V., Tsai, E., Bingley, L., Shaffer, C., Turner, D. L., Runov, A., et al. (2020). The ELFIN mission. *Space Science Reviews*, *216*(5), 103. https://doi.org/10.1007/s11214-020-00721-7

Angelopoulos, V., Zhang, X. J., Artemyev, A. V., Mourenas, D., Tsai, E., Wilkins, C., et al. (2023). Energetic electron precipitation driven by electromagnetic ion cyclotron waves from ELFIN's low altitude perspective. *Space Science Reviews*, *219*(5), 37. https://doi.org/10.1007/s11214-023-00984-w

Artemyev, A. V., Agapitov, O. V., Mozer, F. S., & Spence, H. (2015). Butterfly pitch angle distribution of relativistic electrons in the outer radiation belt: Evidence of nonadiabatic scattering. *Journal of Geophysical Research*, *120*(6), 4279–4297. https://doi.org/10.1002/2014JA020865

Artemyev, A. V., Angelopoulos, V., Runov, A., & Petrukovich, A. A. (2016). Properties of current sheet thinning at $x \sim 10$ to 12 R_E. *Journal of Geophysical Research*, *121*(7), 6718–6731. https://doi.org/10.1002/2016JA022779

Artemyev, A. V., Angelopoulos, V., Zhang, X. J., Chen, L., & Runov, A. (2023). Dispersed relativistic electron precipitation patterns between the ion and electron isotropy boundaries. *Journal of Geophysical Research: Space Physics*, *128*(12), e2023JA032200. https://doi.org/10.1029/2023JA032200

Artemyev, A. V., Angelopoulos, V., Zhang, X. J., Runov, A., Petrukovich, A., Nakamura, R., et al. (2022). Thinning of the magnetotail current sheet inferred from low-altitude observations of energetic electrons. *Journal of Geophysical Research: Space Physics*, *127*(10), e2022JA030705. https://doi.org/10.1029/2022JA030705

Artemyev, A. V., Demekhov, A. G., Zhang, X. J., Angelopoulos, V., Mourenas, D., Fedorenko, Y. V., et al. (2021). Role of ducting in relativistic electron loss by whistler-mode wave scattering. *Journal of Geophysical Research: Space Physics*, *126*(11), e29851. https://doi.org/10.1029/2021JA029851

Artemyev, A. V., Hoshino, M., Lutsenko, V. N., Petrukovich, A. A., Imada, S., & Zelenyi, L. M. (2013). Double power-law spectra of energetic electrons in the Earth magnetotail. *Annales Geophysicae*, *31*(1), 91–106. https://doi.org/10.5194/angeo-31-91-2013

Artemyev, A. V., Neishtadt, A. I., & Angelopoulos, V. (2022). On the role of whistler-mode waves in electron interaction with dipolarizing flux bundles. *Journal of Geophysical Research: Space Physics*, *127*(4), e30265. https://doi.org/10.1029/2022JA030265

Artemyev, A. V., Orlova, K. G., Mourenas, D., Agapitov, O. V., & Krasnoselskikh, V. V. (2013). Electron pitch-angle diffusion: Resonant scattering by waves vs. nonadiabatic effects. *Annales Geophysicae*, *31*(9), 1485–1490. https://doi.org/10.5194/angeo-31-1485-2013

Artemyev, A. V., Zhang, X.-J., Demekhov, A. G., Meng, X., Angelopoulos, V., & Fedorenko, Y. V. (2024). Relativistic electron precipitation driven by mesoscale transients, inferred from ground and multi-spacecraft platforms. *Journal of Geophysical Research: Space Physics*, *129*(2), e2023JA032287. https://doi.org/10.1029/2023JA032287

Birmingham, T. J. (1984). Pitch angle diffusion in the Jovian magnetodisc. *Journal of Geophysical Research*, *89*(A5), 2699–2707. https://doi.org/10.1029/JA089iA05p02699

Boscher, D., Bourdarie, S., O'Brien, P., Guild, T., Heynderickx, D., Morley, S., et al., PRBEM/IRBEM: v5.0.0. (2022). IRBEM contributor community. *Zenodo*. https://doi.org/10.5281/zenodo.6867768

Boudouridis, A., Rodriguez, J. V., Kress, B. T., Dichter, B. K., & Onsager, T. G. (2020). Development of a bowtie inversion technique for real-time processing of the GOES-16/-17 SEISS MPS-HI electron channels. *Space Weather*, *18*(4), e02403. https://doi.org/10.1029/2019SW002403

Büchner, J., & Zelenyi, L. M. (1989). Regular and chaotic charged particle motion in magnetotaillike field reversals. I - Basic theory of trapped motion. *Journal of Geophysical Research*, *94*(A9), 11821–11842. https://doi.org/10.1029/JA094iA09p11821

Capannolo, L., Li, W., & Huang, S. (2022). Identification and classification of relativistic electron precipitation at Earth using supervised deep learning. *Frontiers in Astronomy and Space Sciences*, *9*, 858990. https://doi.org/10.3389/fspas.2022.858990

Capannolo, L., Li, W., Ma, Q., Chen, L., Shen, X. C., Spence, H. E., et al. (2019). Direct observation of subrelativistic electron precipitation potentially driven by EMIC waves. *Geophysical Research Letters*, *46*(22), 12711–12721. https://doi.org/10.1029/2019GL084202

Capannolo, L., Li, W., Ma, Q., Qin, M., Shen, X. C., Angelopoulos, V., et al. (2023). Electron precipitation observed by ELFIN using proton precipitation as a proxy for electromagnetic ion cyclotron (EMIC) waves. *Geophysical Research Letters*, *50*(21), e2023GL103519. https://doi.org/10.1029/2023GL103519

Capannolo, L., Li, W., Millan, R., Smith, D., Sivadas, N., Sample, J., & Shekhar, S. (2022). Relativistic electron precipitation near midnight: Drivers, distribution, and properties. *Journal of Geophysical Research: Space Physics*, *127*(1), e30111. https://doi.org/10.1029/2021JA030111

Carson, B. R., Rodger, C. J., & Clilverd, M. A. (2013). POES satellite observations of EMIC-wave driven relativistic electron precipitation during 1998–2010. *Journal of Geophysical Research: Space Physics*, *118*(1), 232–243. https://doi.org/10.1029/2012JA017998

Chen, H., Gao, X., Lu, Q., & Tsurutani, B. T. (2023). Global distribution of relativistic electron precipitation and the dependences on substorm injection and solar wind ram pressure: Long-term POES observations. *Journal of Geophysical Research: Space Physics*, *128*(11), e2023JA031566. https://doi.org/10.1029/2023JA031566

Chen, H., Gao, X., Lu, Q., Tsurutani, B. T., & Wang, S. (2020). Statistical evidence for EMIC wave excitation driven by substorm injection and enhanced solar wind pressure in the Earth's magnetosphere: Two different EMIC wave sources. *Geophysical Research Letters*, *47*(21), e90275. https://doi.org/10.1029/2020GL090275

Chen, L., Zhang, X.-J., Artemyev, A., Angelopoulos, V., Tsai, E., Wilkins, C., & Horne, R. B. (2022). Ducted chorus waves cause sub-relativistic and relativistic electron microbursts. *Geophysical Research Letters*, *49*(5), e97559. https://doi.org/10.1029/2021GL097559

Chen, L., Zhu, H., & Zhang, X. (2019). Wavenumber analysis of EMIC waves. *Geophysical Research Letters*, *46*(11), 5689–5697. https://doi.org/10.1029/2019GL082686

Chen, R., Gao, X., Lu, Q., Chen, L., Tsurutani, B. T., Li, W., & Wang, S. (2021). In situ observations of whistler mode chorus waves guided by density ducts. *Journal of Geophysical Research: Space Physics*, *126*(4), e28814. https://doi.org/10.1029/2020JA028814

Cohen, I. J., Turner, D. L., Mauk, B. H., Bingham, S. T., Blake, J. B., Fennell, J. F., & Burch, J. L. (2021). Characteristics of energetic electrons near active magnetotail reconnection sites: Statistical evidence for local energization. *Geophysical Research Letters*, *48*(1), e90087. https://doi.org/10.1029/2020GL090087

Constantinescu, O. D., Auster, H.-U., Delva, M., Hillenmaier, O., Magnes, W., & Plaschke, F. (2020). Principal component gradiometer technique for removal of spacecraft-generated disturbances from magnetic field data. *Geoscientific Instrumentation, Methods and Data Systems Discussions*, *25*, 1–26. https://doi.org/10.5194/gi-2020-10

Dubyagin, S., Sergeev, V., Apatenkov, S., Angelopoulos, V., Runov, A., Nakamura, R., et al. (2011). Can flow bursts penetrate into the inner magnetosphere? *Geophysical Research Letters*, *38*(8), 8102. https://doi.org/10.1029/2011GL047016

Dubyagin, S., Sergeev, V. A., & Kubyshkina, M. V. (2002). On the remote sensing of plasma sheet from low-altitude spacecraft. *Journal of Atmospheric and Solar-Terrestrial Physics*, *64*(5–6), 567–572. https://doi.org/10.1016/S1364-6826(02)00014-7

Eriksson, E., Vaivads, A., Alm, L., Graham, D. B., Khotyaintsev, Y. V., & André, M. (2020). Electron acceleration in a magnetotail reconnection outflow region using magnetospheric MultiScale data. *Geophysical Research Letters*, *47*(1), e85080. https://doi.org/10.1029/2019GL085080

Evans, D. S., & Greer, M. S. (2004). *Polar orbiting environmental satellite space environment monitor-2: Instrument description and archive data documentation*. NOAA.

Gao, X., Ma, J., Shao, T., Chen, R., Ke, Y., & Lu, Q. (2023). Why chorus waves are the dominant driver for diffuse auroral precipitation. *Science Bulletin*, *69*(5), 597–600. https://doi.org/10.1016/j.scib.2023.12.009

Grach, V. S., Artemyev, A. V., Demekhov, A. G., Zhang, X.-J., Bortnik, J., & Angelopoulos, V. (2024). Electron precipitation driven by EMIC waves: Two types of energy dispersion. *Geophysical Research Letters*, *51*(9), e2023GL107604. https://doi.org/10.1029/2023GL107604

Grach, V. S., & Demekhov, A. G. (2020). Precipitation of relativistic electrons under resonant interaction with electromagnetic ion cyclotron wave packets. *Journal of Geophysical Research: Space Physics*, *125*(2), e27358. https://doi.org/10.1029/2019JA027358

Grach, V. S., & Demekhov, A. G. (2023). Interaction of relativistic electrons with packets of the electromagnetic ion cyclotron waves of finite length and low amplitude. *Plasma Physics Reports*, *49*(7), 901–911. https://doi.org/10.1134/S1063780X23600561

Hanzelka, M., Li, W., & Ma, Q. (2023). Parametric analysis of pitch angle scattering and losses of relativistic electrons by oblique EMIC waves. *Frontiers in Astronomy and Space Sciences*, *10*, 1163515. https://doi.org/10.3389/fspas.2023.1163515

Hendry, A. T., Rodger, C. J., & Clilverd, M. A. (2017). Evidence of sub-MeV EMIC-driven electron precipitation. *Geophysical Research Letters*, *44*(3), 1210–1218. https://doi.org/10.1002/2016GL071807

Imhof, W. L., Reagan, J. B., & Gaines, E. E. (1977). Fine-scale spatial structure in the pitch angle distributions of energetic particles near the midnight trapping boundary. *Journal of Geophysical Research*, *82*(32), 5215–5221. https://doi.org/10.1029/JA082i032p05215

Imhof, W. L., Reagan, J. B., & Gaines, E. E. (1979). Studies of the sharply defined L dependent energy threshold for isotropy at the midnight trapping boundary. *Journal of Geophysical Research*, *84*(A11), 6371–6384. https://doi.org/10.1029/JA084iA11p06371

Jun, C.-W., Miyoshi, Y., Kurita, S., Yue, C., Bortnik, J., Lyons, L., et al. (2021). The characteristics of EMIC waves in the magnetosphere based on the Van Allen Probes and Arase observations. *Journal of Geophysical Research: Space Physics*, *126*(6), e29001. https://doi.org/10.1029/2020JA029001

Jun, C. W., Yue, C., Bortnik, J., Lyons, L. R., Nishimura, Y., & Kletzing, C. (2019). EMIC wave properties associated with and without injections in the inner magnetosphere. *Journal of Geophysical Research: Space Physics*, *124*(3), 2029–2045. https://doi.org/10.1029/2018JA026279

Ke, Y., Chen, L., Gao, X., Lu, Q., Wang, X., Chen, R., et al. (2021). Whistler mode waves trapped by density irregularities in the Earth's magnetosphere. *Geophysical Research Letters*, *48*(7), e92305. https://doi.org/10.1029/2020GL092305

Khoo, L.-Y., Li, X., Selesnick, R., Schiller, Q., Zhang, K., Zhao, H., et al. (2022). On the challenges of measuring energetic particles in the inner belt: A geant4 simulation of an energetic particle detector instrument, reptile-2. *Journal of Geophysical Research: Space Physics*, *127*(4), e2021JA030249. https://doi.org/10.1029/2021ja030249

Kubyshkina, M., Sergeev, V., Tsyganenko, N., Angelopoulos, V., Runov, A., Donovan, E., et al. (2011). Time-dependent magnetospheric configuration and breakup mapping during a substorm. *Journal of Geophysical Research*, *116*(A5), 0. https://doi.org/10.1029/2010JA015882

Kubyshkina, M., Sergeev, V., Tsyganenko, N., Angelopoulos, V., Runov, A., Singer, H., et al. (2009). Toward adapted time-dependent magnetospheric models: A simple approach based on tuning the standard model. *Journal of Geophysical Research*, *114*(A1), 0. https://doi.org/10.1029/2008JA013547

Li, W., Bortnik, J., Thorne, R. M., & Angelopoulos, V. (2011). Global distribution of wave amplitudes and wave normal angles of chorus waves using THEMIS wave observations. *Journal of Geophysical Research*, *116*(A12), 12205. https://doi.org/10.1029/2011JA017035

Li, W., & Hudson, M. K. (2019). Earth's Van Allen radiation belts: From discovery to the Van Allen Probes era. *Journal of Geophysical Research: Space Physics*, *124*(11), 8319–8351. https://doi.org/10.1029/2018JA025940

Li, W., Ni, B., Thorne, R. M., Bortnik, J., Green, J. C., Kletzing, C. A., et al. (2013). Constructing the global distribution of chorus wave intensity using measurements of electrons by the POES satellites and waves by the Van Allen Probes. *Geophysical Research Letters*, *40*, 4526–4532. https://doi.org/10.1002/grl.50920

Li, X. (2024). Unveiling energetic particle dynamics in the near-Earth environment from cubesat missions. *AGU Advances*, *5*(3), e2024AV001256. https://doi.org/10.1029/2024av001256

Li, X., Kohnert, R., Palo, S., Selesnick, R., Khoo, L., Schiller, Q., et al. (2022). Two generations of CubeSat missions (CSSWE and CIRBE) to take on the challenges of measuring relativistic electrons in the Earth's magnetosphere.

Li, X., Palo, S., Kohnert, R., Gerhardt, D., Blum, L., Schiller, Q., et al. (2012). Colorado student space weather experiment: Differential flux measurements of energetic particles in a highly inclined low Earth orbit. *Dynamics of the Earth's Radiation Belts and Inner Magnetosphere*, *199*, 385–404. https://doi.org/10.1029/2012gm001313

Li, X., Selesnick, R., Mei, Y., O'Brien, D., Hogan, B., Xiang, Z., et al. (2024). First results from REPTile-2 measurements onboard CIRBE. *Geophysical Research Letters*, *51*(3), e2023GL107521. https://doi.org/10.1029/2023GL107521

Li, X., Selesnick, R., Schiller, Q., Zhang, K., Zhao, H., Baker, D. N., & Temerin, M. A. (2017). Measurement of electrons from albedo neutron decay and neutron density in near-Earth space. *Nature*, *552*(7685), 382–385. https://doi.org/10.1038/nature24642

Lin, Y., Wang, X. Y., Lu, S., Perez, J. D., & Lu, Q. (2014). Investigation of storm time magnetotail and ion injection using three-dimensional global hybrid simulation. *Journal of Geophysical Research*, *119*(9), 7413–7432. https://doi.org/10.1002/2014JA020005

Magnes, W., Hillenmaier, O., Auster, H. U., Brown, P., Kraft, S., Seon, J., et al. (2020). Space weather magnetometer aboard GEO-KOMPSAT-2A. *Space Science Reviews*, *216*(8), 119. https://doi.org/10.1007/s11214-020-00742-2

Millan, R., Sample, J., Sotirelis, T., McCarthy, M., Woodger, L., Shih, A. Y., et al. (2022). New missions for understanding electron microburst precipitation. In *44th COSPAR scientific assembly. Held 16–24 July* (Vol. 44, p. 3327).

Millan, R., Sample, J., Sotirelis, T., Woodger, L., Li, W., Capannolo, L., & Cantwell, K. (2021). The relativistic electron atmospheric loss CubeSat. *Agu fall meeting abstracts*, *2021*, SM55D–1810.

Millan, R. M., & Thorne, R. M. (2007). Review of radiation belt relativistic electron losses. *Journal of Atmospheric and Solar-Terrestrial Physics*, *69*(3), 362–377. https://doi.org/10.1016/j.jastp.2006.06.019

Miyoshi, Y., Sakaguchi, K., Shiokawa, K., Evans, D., Albert, J., Connors, M., & Jordanova, V. (2008). Precipitation of radiation belt electrons by emic waves, observed from ground and space. *Geophysical Research Letters*, *35*(23), L23101. https://doi.org/10.1029/2008GL035727

Mourenas, D., Artemyev, A. V., Zhang, X. J., Angelopoulos, V., Tsai, E., & Wilkins, C. (2021). Electron lifetimes and diffusion rates inferred from ELFIN measurements at low altitude: First results. *Journal of Geophysical Research: Space Physics*, *126*(11), e29757. https://doi.org/10.1029/2021JA029757

Murase, K., Kataoka, R., Nishiyama, T., Nishimura, K., Hashimoto, T., Tanaka, Y., et al. (2022). Mesospheric ionization during substorm growth phase. *Journal of Space Weather and Space Climate*, *12*, 18. https://doi.org/10.1051/swsc/2022012

Nakamura, S., Miyoshi, Y., Shiokawa, K., Omura, Y., Mitani, T., Takashima, T., et al. (2022). Simultaneous observations of emic-induced drifting electron holes (EDEHs) in the Earth's radiation belt by the Arase satellite, Van Allen Probes, and THEMIS. *Geophysical Research Letters*, *49*(5), e2021GL095194. https://doi.org/10.1029/2021gl095194

Newell, P. T., Sergeev, V. A., Bikkuzina, G. R., & Wing, S. (1998). Characterizing the state of the magnetosphere: Testing the ion precipitation maxima latitude (b2i) and the ion isotropy boundary. *Journal of Geophysical Research*, *103*(A3), 4739–4746. https://doi.org/10.1029/97JA03622

Panov, E. V., Baumjohann, W., Nakamura, R., Pritchett, P. L., Weygand, J. M., & Kubyshkina, M. V. (2019). Ionospheric footprints of detached magnetotail interchange heads. *Geophysical Research Letters*, *46*(13), 7237–7247. https://doi.org/10.1029/2019GL083070

Panov, E. V., & Pritchett, P. L. (2018). Dawnward drifting interchange heads in the Earth's magnetotail. *Geophysical Research Letters*, *45*(17), 8834–8843. https://doi.org/10.1029/2018GL078482

Schiller, Q., Li, X., Blum, L., Tu, W., Turner, D. L., & Blake, J. (2014). A nonstorm time enhancement of relativistic electrons in the outer radiation belt. *Geophysical Research Letters*, *41*(1), 7–12. https://doi.org/10.1002/2013gl058485

Sergeev, V. A., Angelopoulos, V., Kubyshkina, M., Donovan, E., Zhou, X.-Z., Runov, A., et al. (2011). Substorm growth and expansion onset as observed with ideal ground-spacecraft THEMIS coverage. *Journal of Geophysical Research*, *116*(A5), A00I26. https://doi.org/10.1029/2010JA015689

Sergeev, V. A., Chernyaev, I. A., Angelopoulos, V., & Ganushkina, N. Y. (2015). Magnetospheric conditions near the equatorial footpoints of proton isotropy boundaries. *Annales Geophysicae*, *33*(12), 1485–1493. https://doi.org/10.5194/angeo-33-1485-2015

Sergeev, V. A., Chernyaev, I. A., Angelopoulos, V., Runov, A. V., & Nakamura, R. (2014). Stopping flow bursts and their role in the generation of the substorm current wedge. *Geophysical Research Letters*, *41*(4), 1106–1112. https://doi.org/10.1002/2014GL059309

Sergeev, V. A., Gordeev, E. I., Merkin, V. G., & Sitnov, M. I. (2018). Does A local B-minimum appear in the tail current sheet during a substorm growth phase? *Geophysical Research Letters*, *45*(6), 2566–2573. https://doi.org/10.1002/2018GL077183

Sergeev, V. A., Kubyshkina, M. V., Semenov, V. S., Artemyev, A., Angelopoulos, V., & Runov, A. (2023). Unusual magnetospheric dynamics during intense substorm initiated by strong magnetospheric compression. *Journal of Geophysical Research: Space Physics*, *128*(11), e2023JA031536. https://doi.org/10.1029/2023JA031536

Sergeev, V. A., Malkov, M., & Mursula, K. (1993). Testing the isotropic boundary algorithm method to evaluate the magnetic field configuration in the tail. *Journal of Geophysical Research*, *98*(A5), 7609–7620. https://doi.org/10.1029/92JA02587

Sergeev, V. A., Nishimura, Y., Kubyshkina, M., Angelopoulos, V., Nakamura, R., & Singer, H. (2012). Magnetospheric location of the equatorward prebreakup arc. *Journal of Geophysical Research: Space Physics*, *117*(A1), A01212. https://doi.org/10.1029/2011JA017154

Sergeev, V. A., Sazhina, E. M., Tsyganenko, N. A., Lundblad, J. A., & Soraas, F. (1983). Pitch-angle scattering of energetic protons in the magnetotail current sheet as the dominant source of their isotropic precipitation into the nightside ionosphere. *Planatary Space Science*, *31*(10), 1147–1155. https://doi.org/10.1016/0032-0633(83)90103-4

Sheeley, B. W., Moldwin, M. B., Rassoul, H. K., & Anderson, R. R. (2001). An empirical plasmasphere and trough density model: CRRES observations. *Journal of Geophysical Research*, *106*(A11), 25631–25642. https://doi.org/10.1029/2000JA000286

Shekhar, S., Millan, R., & Smith, D. (2017). A statistical study of the spatial extent of relativistic electron precipitation with polar orbiting environmental satellites. *Journal of Geophysical Research: Space Physics*, *122*(11), 11274–11284. https://doi.org/10.1002/2017JA024716

Shekhar, S., Millan, R. M., & Hudson, M. K. (2018). A statistical study of spatial variation of relativistic electron precipitation energy spectra with polar operational environmental satellites. *Journal of Geophysical Research: Space Physics*, *123*(5), 3349–3359. https://doi.org/10.1002/2017JA025041

Shi, R., Summers, D., Ni, B., Fennell, J. F., Blake, J. B., Spence, H. E., & Reeves, G. D. (2016). Survey of radiation belt energetic electron pitch angle distributions based on the Van Allen Probes MagEIS measurements. *Journal of Geophysical Research: Space Physics*, *121*(2), 1078–1090. https://doi.org/10.1002/2015JA021724

Shi, X., Stephens, G. K., Artemyev, A. V., Sitnov, M. I., & Angelopoulos, V. (2024). Picturing global substorm dynamics in the magnetotail using low-altitude ELFIN measurements and data mining-based magnetic field reconstructions. *arXiv e-prints*, *22*(10). arXiv:2406.13143. https://doi.org/10.48550/arXiv.2406.13143

Shprits, Y. Y., Subbotin, D. A., Meredith, N. P., & Elkington, S. R. (2008). Review of modeling of losses and sources of relativistic electrons in the outer radiation belt II: Local acceleration and loss. *Journal of Atmospheric and Solar-Terrestrial Physics*, *70*(14), 1694–1713. https://doi.org/10.1016/j.jastp.2008.06.014

Silin, I., Mann, I. R., Sydora, R. D., Summers, D., & Mace, R. L. (2011). Warm plasma effects on electromagnetic ion cyclotron wave MeV electron interactions in the magnetosphere. *Journal of Geophysical Research: Space Physics*, *116*(A5), A05215. https://doi.org/10.1029/2010JA016398

Sitnov, M. I., Stephens, G. K., Tsyganenko, N. A., Miyashita, Y., Merkin, V. G., Motoba, T., et al. (2019). Signatures of nonideal plasma evolution during substorms obtained by mining multimission magnetometer data. *Journal of Geophysical Research: Space Physics*, *124*(11), 8427–8456. https://doi.org/10.1029/2019JA027037

Sivadas, N., Semeter, J., Nishimura, Y., & Mrak, S. (2019). Optical signatures of the outer radiation belt boundary. *Geophysical Research Letters*, *46*(15), 8588–8596. https://doi.org/10.1029/2019GL083908

Sorathia, K. A., Merkin, V. G., Panov, E. V., Zhang, B., Lyon, J. G., Garretson, J., et al. (2020). Ballooning-interchange instability in the near-Earth plasma sheet and auroral beads: Global magnetospheric modeling at the limit of the MHD approximation. *Geophysical Research Letters*, *47*(14), e88227. https://doi.org/10.1029/2020GL088227

Stephens, G. K., Sitnov, M. I., Korth, H., Tsyganenko, N. A., Ohtani, S., Gkioulidou, M., & Ukhorskiy, A. Y. (2019). Global empirical picture of magnetospheric substorms inferred from multimission magnetometer data. *Journal of Geophysical Research: Space Physics*, *124*(2), 1085–1110. https://doi.org/10.1029/2018JA025843

Stephens, G. K., Sitnov, M. I., Ukhorskiy, A. Y., Roelof, E. C., Tsyganenko, N. A., & Le, G. (2016). Empirical modeling of the storm time innermost magnetosphere using Van Allen Probes and THEMIS data: Eastward and banana currents. *Journal of Geophysical Research*, *121*(1), 157–170. https://doi.org/10.1002/2015JA021700

Summers, D., & Thorne, R. M. (2003). Relativistic electron pitch-angle scattering by electromagnetic ion cyclotron waves during geomagnetic storms. *Journal of Geophysical Research*, *108*(A4), 1143. https://doi.org/10.1029/2002JA009489

Tan, X., Dunlop, M. W., Dong, X. C., Yang, Y. Y., Du, Y. S., Shen, C., et al. (2023). Ring current morphology from MMS observations. *Journal of Geophysical Research: Space Physics*, *128*(4), e2023JA031372. https://doi.org/10.1029/2023JA031372

Thébault, E., Finlay, C. C., Beggan, C. D., Alken, P., Aubert, J., Barrois, O., et al. (2015). International geomagnetic reference field: The 12th generation. *Earth Planets and Space*, *67*, 1–19. https://doi.org/10.1186/s40623-015-0228-9

Thorne, R. M., Bortnik, J., Li, W., & Ma, Q. (2021). Wave–particle interactions in the Earth's magnetosphere. In *Magnetospheres in the solar system* (pp. 93–108). American Geophysical Union (AGU). https://doi.org/10.1002/9781119815624.ch6

Tsai, E., Artemyev, A., Angelopoulos, V., & Zhang, X.-J. (2023). Investigating whistler-mode wave intensity along field lines using electron precipitation measurements. *Journal of Geophysical Research: Space Physics*, *128*(8), e2023JA031578. https://doi.org/10.1029/2023JA031578

Tsai, E., Artemyev, A., Zhang, X.-J., & Angelopoulos, V. (2022). Relativistic electron precipitation driven by nonlinear resonance with whistler-mode waves. *Journal of Geophysical Research: Space Physics*, *127*(5), e30338. https://doi.org/10.1029/2022JA030338

Turner, D. L., Cohen, I. J., Michael, A., Sorathia, K., Merkin, S., Mauk, B. H., et al. (2021). Can Earth's magnetotail plasma sheet produce a source of relativistic electrons for the radiation belts? *Geophysical Research Letters*, *48*(21), e95495. https://doi.org/10.1029/2021GL095495

Vallat, C., Dandouras, I., Dunlop, M., Balogh, A., Lucek, E., Parks, G. K., et al. (2005). First current density measurements in the ring current region using simultaneous multi-spacecraft CLUSTER-FGM data. *Annales Geophysicae*, *23*(5), 1849–1865. https://doi.org/10.5194/angeo-23-1849-2005

Wilkins, C., Angelopoulos, V., Runov, A., Artemyev, A., Zhang, X. J., Liu, J., & Tsai, E. (2023). Statistical characteristics of the electron isotropy boundary. *Journal of Geophysical Research: Space Physics*, *128*(10), e2023JA031774. https://doi.org/10.1029/2023JA031774

Yahnin, A. G., Yahnina, T. A., Raita, T., & Manninen, J. (2017). Ground pulsation magnetometer observations conjugated with relativistic electron precipitation. *Journal of Geophysical Research: Space Physics*, *122*(9), 9169–9182. https://doi.org/10.1002/2017JA024249

Yahnin, A. G., Yahnina, T. A., Semenova, N. V., Gvozdevsky, B. B., & Pashin, A. B. (2016). Relativistic electron precipitation as seen by NOAA POES. *Journal of Geophysical Research: Space Physics*, *121*(9), 8286–8299. https://doi.org/10.1002/2016JA022765

Yando, K., Millan, R. M., Green, J. C., & Evans, D. S. (2011). A Monte Carlo simulation of the NOAA POES medium energy proton and electron detector instrument. *Journal of Geophysical Research*, *116*(A10). https://doi.org/10.1029/2011ja016671

Young, S. L., Denton, R. E., Anderson, B. J., & Hudson, M. K. (2008). Magnetic field line curvature induced pitch angle diffusion in the inner magnetosphere. *Journal of Geophysical Research*, *113*(A3), 3210. https://doi.org/10.1029/2006JA012133

Zhang, K., Li, X., Schiller, Q., Gerhardt, D., Zhao, H., & Millan, R. (2017). Detailed characteristics of radiation belt electrons revealed by CSSWE/reptile measurements: Geomagnetic activity response and precipitation observation. *Journal of Geophysical Research: Space Physics*, *122*(8), 8434–8445. https://doi.org/10.1002/2017ja024309

Zhang, K., Li, X., Xiang, Z., Khoo, L. Y., Zhao, H., Looper, M. D., et al. (2020). Long-term variations of quasi-trapped and trapped electrons in the inner radiation belt observed by demeter and sampex. *Journal of Geophysical Research: Space Physics*, *125*(9), e2020JA028086. https://doi.org/10.1029/2020ja028086

Zhang, X.-J., Angelopoulos, V., Mourenas, D., Artemyev, A., Tsai, E., & Wilkins, C. (2022). Characteristics of electron microburst precipitation based on high-resolution elfin measurements. *Journal of Geophysical Research: Space Physics*, *127*(5), e2022JA030509. https://doi.org/10.1029/2022ja030509

Zhao, H., Friedel, R. H. W., Chen, Y., Reeves, G. D., Baker, D. N., Li, X., et al. (2018). An empirical model of radiation belt electron pitch angle distributions based on Van Allen Probes measurements. *Journal of Geophysical Research: Space Physics*, *123*(5), 3493–3511. https://doi.org/10.1029/2018JA025277

Zou, Y., Zhang, X.-J., Artemyev, A. V., Shen, Y., & Angelopoulos, V. (2024). The key role of magnetic curvature scattering in energetic electron precipitation during substorms. *Geophysical Research Letters*, *51*(14), e2024GL109227. https://doi.org/10.1029/2024GL109227